

# Binary Quasars Observed by Chandra

Paul J. Green<sup>1,2</sup>

pgreen@cfa.harvard.edu

Adam D. Myers<sup>2,3</sup>, Wayne A. Barkhouse<sup>2,4</sup>, Thomas L. Aldcroft<sup>1</sup>, Markos Trichas<sup>1</sup> & Ángel Ruiz<sup>5</sup>

## ABSTRACT

We present analysis of Chandra X-ray imaging and spectroscopy for a sample of 14 quasars in spatially-resolved pairs. The pairs were all targeted as part of a complete sample of binary quasar candidates with small transverse separations drawn from Sloan Digital Sky Survey (SDSS) DR6 photometry. One pair, SDSS J1254+0846 at  $z=0.44$ , discussed in detail in a companion paper, clearly inhabits an ongoing, pre-coalescence galaxy merger showing obvious tidal tails. We measure the distribution of X-ray and optical-to-X-ray power-law indices in these binary quasars, and find no significant difference with large control samples of isolated quasars. The sample also provides an unusual opportunity to examine whether the much-studied  $\alpha_{\text{ox}}(l_{2500\text{\AA}})$  correlation among ensembles of isolated QSOs persists in QSOs identically matched in redshift and environment. QSOs within these physical pairs are not inconsistent with the global trend. We present near-IR imaging and photometry from MMT with SWIRC, and fit simple spectral energy distributions to all 14 QSOs, and find preliminary evidence that substantial contributions from star formation are required. Sensitive searches of the X-ray images for extended emission, and the optical images for optical galaxy excess show that binary QSOs, while likely occurring in strong peaks of the dark matter distribution, are not preferentially found in rich cluster environments. We

---

<sup>1</sup>Harvard-Smithsonian Center for Astrophysics, 60 Garden Street, Cambridge MA 02138

<sup>2</sup>Visiting Astronomer, Kitt Peak National Observatory and Cerro Tololo Inter-American Observatory, National Optical Astronomy Observatory, which is operated by the Association of Universities for Research in Astronomy, Inc. (AURA) under cooperative agreement with the National Science Foundation.

<sup>3</sup>Department of Astronomy, University of Illinois at Urbana-Champaign, 1002 West Green Street, Urbana, IL 61801-3080

<sup>4</sup>Department of Physics, University of North Dakota, Grand Forks, ND 58202

<sup>5</sup>Instituto de Física de Cantabria (IFCA), CSIC-UC, Avda. de los Castros, 39005 Santander, Spain

present in our Appendix a potentially useful primer on X-ray flux and luminosity calculations.

*Subject headings:* black hole physics; galaxies: active; galaxies: interactions; galaxies: nuclei quasars: emission lines

## Contents

|          |  |           |
|----------|--|-----------|
| <b>1</b> | <b>Introduction</b>                      | <b>2</b>  |
| <b>2</b> | <b>Binary Quasar Sample</b>              | <b>5</b>  |
| <b>3</b> | <b>Chandra X-ray Observations</b>        | <b>6</b>  |
| <b>4</b> | <b>Optical Imaging</b>                   | <b>8</b>  |
| <b>5</b> | <b>Near Infrared Imaging</b>             | <b>10</b> |
| <b>6</b> | <b>Comparison to Single Quasars</b>      | <b>11</b> |
| 6.1      | Comparing $\alpha_{\text{ox}}$ . . . . . | 12        |
| <b>7</b> | <b>Spectral Energy Distributions</b>     | <b>14</b> |
| <b>8</b> | <b>Conclusions</b>                       | <b>15</b> |

## 1. Introduction

Luminous quasars have always inhabited a relatively small fraction of galaxies. Studies of the clustering properties of quasars (two-point correlation functions; Croom et al. 2005; Myers et al. 2006, 2007a; Shen et al. 2010a) indicate that quasars inhabit rare massive dark matter halos ( $M_{\text{halo}} \gtrsim 10^{12} h^{-1} M_{\odot}$ ) and that their bias relative to the underlying matter increases rapidly with redshift (Ross et al. 2009). Quasars with a close ( $< 1$  Mpc) quasar companion at comparable luminosity constitute only  $\sim 0.1\%$  of quasars overall, but that represents a strong excess on small scales over the extrapolation from the larger scale QSO

correlation function (Hennawi et al. 2006; Myers et al. 2008; Hennawi et al. 2010; Shen et al. 2010a). Indeed, the surprisingly large number of binary quasars in the universe (Djorgovski et al. 1987; Myers et al. 2007b; Hennawi et al. 2006) is a key underpinning of the merger hypothesis. Many authors (Kochanek et al. 1999; Mortlock et al. 1999; Myers et al. 2007b) have noted that an excess of binary quasars could be due to tidal forces in dissipative mergers that trigger inflow of gas towards the nuclear region, and hence strong accretion activity in the nuclei of merging galaxies. However, it is not known whether mergers the *cause* of the observed excess of binary quasars or rather is the excess of binary quasars the *result* of enhanced small-scale clustering for the merger-prone halos that host quasars? The measured small-scale excess including binary quasars ( $R \lesssim 100$  kpc) may *not* be due to mutual triggering, but rather simply a statistically predictable consequence of locally overdense environments (Hopkins et al. 2008). These questions motivate detailed studies of binary AGN.

At high redshifts, where the merging process is likely to be efficient (e.g., Springel 2005), binary AGN are difficult to resolve. At more recent epochs, where they could be resolved, the merger rate is lower (Hopkins et al. 2008). Nearby examples exist, however. The merger hypothesis is supported by the existence of spatially-resolved binary active galactic nuclei (AGN) in a few  $z < 0.1$  galaxies with one or both of the nuclei heavily obscured in X-rays (NGC 6240, Komossa et al. 2003; Arp 299, Zezas et al. 2003; Mrk 463, Bianchi et al. 2008), by the unusual BL Lac-type object OJ 287 (Sillanpaa et al. 1988; Valtonen et al. 2009), and perhaps by X-shaped morphology in radio galaxies (e.g., Merritt & Ekers 2002; Liu 2004; Cheung 2007). In addition, CXOC J100043.1+020637 contains two AGN resolved at  $0.5''$  ( $\sim 2.5$  kpc) separation in HST/ACS imaging, which have a radial velocity difference of  $\Delta v = 150$  km/s, and appear to be hosted by a galaxy with a tidal tail (Comerford et al. 2009; Civano et al. 2010).

A recent flurry of results from searches for candidate close binary AGN (with sub-kpc projected separations) has mostly involved spectroscopic (unresolved) binaries. Some show both broad and narrow emission lines with significant velocity offsets, such as SDSS J153636.22+1044127.0 (Boroson & Lauer 2009), SDSS J105041.35+345631.3 (Shields et al. 2009), or SDSS J092712.65+294344.0 (Komossa et al. 2008). Some may be true binary SMBH, perhaps including SMBH that have been “kicked” due to anisotropic emission of gravitational radiation near coalescence. Some may be similar to spatially unresolved quasars with double-peaked broad emission lines (e.g., Strateva et al. 2003). Debate surrounding the various interpretations persists (e.g., Chornock et al. 2010; Lauer & Boroson 2009; Wrobel & Laor 2009; Tang & Grindlay 2009; Vivek et al. 2009). Many spectroscopic binary AGN candidates with narrow emission lines only have been selected from the SDSS based on double-peaked [O III]  $\lambda\lambda 4959, 5007$  emission lines in their fiber spectra (Wang et al. 2009; Smith et al. 2010; Liu et al. 2010). Some remarkable objects have been found (e.g., Xu & Komossa 2009), but several scenarios can produce

double-peaked narrow emission lines, including projection effects, outflows, jet-cloud interactions, special narrow-line region (NLR) geometries, or a merger where one AGN illuminates two NLRs. Near-infrared (near-IR) imaging and optical slit spectroscopy can reveal genuine double-nuclei (Liu et al. 2010), which constitute only about 10% of the candidates (Shen et al. 2010b).

Spatially-resolved, confirmed mergers of broad line AGN may well be the most useful for tracing the physics of the early merger process because they probe *ongoing* mergers, and because the spatial and velocity information, especially when combined with well-resolved spectra providing separate black hole mass estimates, offer more constraints on the properties of the merging components and the evolution of the merger. Examples of resolved binary AGN in confirmed mergers are virtually unknown. Probably the best example to date is SDSS J1254+0846 (Green et al. 2010), which clearly shows tidal tails from the ongoing merger. Spatially-resolved active binary mergers such as these provide by far the strongest constraints on merger physics at kiloparsec scales. Even when such obvious merger signatures are not available, other probes of the properties of binary quasars such as their environments, spectral energy distributions, nuclear and host galaxy properties provide useful information to help distinguish which may be undergoing merging or triggering, and to elucidate merger physics itself.

In this paper, we probe the multi-wavelength properties of a small but uniform sample of binary quasars, described in §2. Using Chandra X-ray imaging and spectral constraints, we study in §3 the high-energy SEDs of binary quasars and also look for evidence of any local hot ICM indicating a host group or cluster). X-ray cluster detection avoids some of the pitfalls of optical/IR selection: projection effects and red sequence bias towards evolved galaxy populations. Our X-ray imaging is sensitive even to poor clusters and groups with high  $M/L$  (Barkhouse et al. 2006), even in the presence of bright quasar point sources (Green 2005). We have also obtained optical imaging with the NOAO/4m-MOSAIC on Kitt Peak which we present in §4, to look for local galaxy overdensities, and to study deeper imaging of the quasars themselves in a search for signs of merger activity. In §5 we further present deep IR imaging we have obtained at Mt Hopkins using the SAO Wide-field InfraRed Camera (SWIRC) on the 6.5m MMT, to further examine the SEDs of binary QSOs. Template-fitting to these SEDS presented in §7 will allow us to contrast binary QSOs directly with a large ChaMP sample of isolated QSOs in an upcoming paper. In §6, we contrast the X-ray and optical properties of binary QSOs to a subset of QSOs imaged in X-rays by *Chandra* as part of the *Chandra* Multiwavelength Project (Green et al. 2004; Green et al. 2009). We present our conclusions in §8.

Throughout, we assume the following cosmological parameters for distance-dependent

quantities:  $\Omega_m = 0.3$ ,  $\Omega_\Lambda = 0.7$ , and  $H_0 = 72 \text{ km s}^{-1} \text{ Mpc}^{-1}$ .

## 2. Binary Quasar Sample

Ongoing mergers hosting two luminous AGN are rare, so while a handful of serendipitous examples exist, huge volumes of sky must be searched to find them systematically. The Sloan Digital Sky Survey (SDSS; York et al. 2000) provides a large sample of multicolor imaging and spectroscopy for this purpose.

The objects in our sample were targeted as as part of a complete sample of binary quasar candidates with small transverse separations drawn from SDSS DR6 photometry (Myers et al. 2011, in preparation). A preliminary targeted follow-up campaign of such objects (for DR4) is discussed in Myers et al. (2008). Quasar candidates were selected as having  $g < 20.85$  and either the “UVX quasar” and/or “low-redshift quasar” Bayesian classification flags set in the catalog of Richards et al. (2009).<sup>1</sup> These cuts ensure a high efficiency of quasar pairs in the targets and a reasonably homogeneous sample over redshifts of  $0.4 < z < 2.4$ . Pairs of quasar candidates were then followed up spectroscopically if they had an angular separation of  $3''$  to  $6''$ . To extend the completeness of the sample as a function of comoving separation, the sample was also extended to pairs with separations of  $6''$  to  $\sim 7.7''$  if neither component had a known redshift at  $z > 1.2$ .

Our uniform parent sample further allows us to place these systems in their larger cosmological context, which is crucial if we are to understand the role of merger-triggered supermassive black hole accretion, and its relationship to galaxy evolution. By selection, these quasar pairs are likely to have a wide projected sky projection, which makes them useful for providing morphological constraints on merger models.

Following an extensive observational campaign with the R-C Spectrograph on the Mayall 4-m at Kitt Peak National Observatory and the Double Spectrograph on the 200-inch Hale telescope at Palomar Observatory, the sample of target quasar pairs from which our Chandra subsample was drawn is now complete (again, see Myers et al. 2011, in preparation).

We proposed for Chandra time to observe a subsample of SDSS binary quasar pairs using the homogeneous selection criteria of Myers et al. (2008), restricted to velocity differences  $\Delta v < 800 \text{ km s}^{-1}$  and separations  $R_p < 30 \text{ kpc}$ . The separation criterion selects hosts likely to be interacting on their first or second pass. The velocity criterion removes most chance projections but still allows for hosts in a variety of environments from isolated pairs to

---

<sup>1</sup>uvxts=1 OR lowzts=1

massive clusters. To construct a pilot sample approaching statistical size, without requiring excessive exposure, we further restricted our sample to 7 pairs with  $z < 1$ , whose properties are shown in Tables 1 and 2.

### 3. Chandra X-ray Observations

We obtained X-ray images of the seven quasar pairs with the Chandra X-ray Observatory on the dates shown in Table 1. We placed targets near the ACIS-S aimpoint, and tuned our exposure times to achieve  $\sim 100$  counts for the fainter member of each pair, by converting the SDSS  $r$  mag to an expected  $f_X$  using the 75th percentile X-ray-faintest value of  $\log(f_X/f_r) = -0.5$  from the Chandra Multiwavelength Project (ChAMP) QSO sample (Green et al. 2009)). For every pair, we convert  $f_X$  to ACIS-S counts/sec using PIMMS, with  $\Gamma = 1.9$  through  $N_H^{Gal}$ , and derive the exposure, which yielded exposure times from 12 to 30 ksec, with a total of  $\sim 172$  ksec.

The small ( $2\text{--}3''$ ) separation of 3 of these pairs is not too serious a challenge for Chandra. In all cases but one, the X-ray components are detected, well-resolved by Chandra, and correspond closely ( $< 0.2''$ ) to their SDSS counterparts. To avoid cross-contamination, we extracted the X-ray photons from apertures corresponding to 90% of the counts (for 1.5 keV). Some of the QSOs in our sample yielded relatively few net counts. In such cases, instrumental hardness ratios are often used, in the belief that genuine spectral fitting is not warranted by the data quality. We stress however that spectral fitting provides the most consistent and robust estimates of the physical parameters of interest, the power law slope and intrinsic absorption.

SDSS J160602.81+290048.7 was not detected using `wavdetect` and a detection significance threshold corresponding to about one false source per ACIS chip. However, aperture photometry at the optical source position shows 6 net counts, all above 2 keV.

We fit an X-ray power-law spectral model

$$N(E) = N(E_0) \left(\frac{E}{E_0}\right)^{(1-\Gamma)} \exp[-N_H^{Gal}\sigma(E) - N_H^z\sigma(E(1+z))]$$

to the counts for each QSO using the CIAO tool *Sherpa*, where  $N(E_0)$  is the normalization in photons  $\text{cm}^{-2} \text{sec}^{-1} \text{keV}^{-1}$  at a reference energy  $E_0$  (of 1 keV here), and  $\sigma(E)$  is the absorption cross-section (Morrison & McCammon 1983; Wilms et al. 2000). We fix  $N_H^{Gal}$  at the appropriate Galactic neutral absorbing column taken from Dickey & Lockam (1990), and perform (1) a simple power-law fit with no intrinsic absorption component (model *PL*) and (2) include an intrinsic absorber with neutral column  $N_H^z$  at the source redshift (model

*PLAbs*). Unbinned spectra were fit using Cash statistics (Cash 1979). The best-fit model parameters for all components are shown in Table 2.

The  $\Gamma$  power-law energy index values we find are typical of SDSS Type 1 QSOs in general (Green et al. 2009), with a mean of  $2.14 \pm 0.29$  and a median of 2.11. Unabsorbed fluxes and luminosities are calculated as detailed in the Appendix, using the  $\Gamma$  values from the *PLAbs* fits in every case except for SDSS J160602.81+290048.7, where we assume  $\Gamma=1.8$ . These values only differ substantially from the *PL*-only fit values in the two cases where there is absorption detected at  $>68\%$  confidence.

Only Chandra can resolve these quasar pairs in X-rays and still detect a typical host cluster. To insure that we can always detect clusters as weak as  $\sim 0.1 L_X^*$  ( $L_{0.5-2\text{keV}} \gtrsim 3 \times 10^{43}$ ; Mullis et al. 2004), we have slightly increased our exposure times from the above formula for the two pairs SDSSJ0740 (+5 ksec) and SDSSJ1606 (+6 ksec). Despite the presence of bright quasar emission, we know (Green et al. 2002; Aldcroft & Green 2003) that we can thereby detect extended cluster emission against a typical ACIS-S background with  $\sim 50$  diffuse counts or more in any our fields.

Significant extended X-ray emission is clearly visible in the ACIS image of SDSS J1158+1235 (obsid 10314), but it is  $43''$  SSW of the QSO pair’s midpoint. The peak of the extended X-ray emission is coincident with a luminous  $i = 17.18$  absorption line galaxy at  $z = 0.2652$ , SDSS J115821.96+123438.6. At absolute magnitude  $M_i \sim -23.71$ , this is clearly the cD galaxy of an X-ray cluster. Using a circular aperture of  $24''$  radius for the cluster, and a background annulus from  $62 - 110''$  excluding all detected source regions, we derive  $301 \pm 19$  counts from the cluster. Assuming a Raymond-Smith plasma with  $T = 2\text{keV}$  and metallicity 0.2 solar, we derive  $f(0.5-2\text{keV}) = 3.97 \times 10^{-14} \text{erg cm}^{-2} \text{s}^{-1}$ , and a luminosity of  $8.2 \times 10^{42} \text{erg s}^{-1}$ .

Otherwise, no significant extended emission sources are evident to the eye on the ACIS-S3 images in the immediate neighborhood of the QSO pairs. When searching for faint extended sources, however, it is important to minimize background contamination. The ACIS particle background increases significantly below  $0.5\text{keV}$  and again at high energies. To optimize detection and visual inspection of possible weak cluster emission, we first filtered the cleaned image to include only photons between  $0.5$  and  $2\text{keV}$ . Around the QSO positions as detected by *wavdetect*, we masked out pixels within twice the radius that encompasses 95% of the encircled energy. (The 95% PSF radius at  $1.5\text{keV}$  is about  $2.06''$ .) For visual inspection, we also excised regions around all other detected sources, corresponding to 4 times the  $4\sigma$  Gaussian source region output of *wavdetect*.

We then generated 7 annuli of  $50\text{kpc}$  annular projected width each, starting at  $R =$

75 kpc from the mean of the detected QSO coordinates.<sup>2</sup> Though the sample redshifts range from 0.44 to 0.978, these radii only differ slightly between the targets (dispersion in the mean is about 13%), so we used a single set of six 7'' annuli from 10 to 52''. We set a background annulus from 60 – 110'', and calculated radial surface brightness profiles.

There are just 2 fields with radial profiles that rise consistently towards the QSOs. For SDSS J0740+2926 (obsid 10312), the profile arises from some faint diffuse emission with a centroid about 7.5'' NW of the mean QSO positions. The emission only encompasses about  $9.8 \pm 3.6$  net (0.5-2 keV) counts, and there is at least one other such source in the field, so we discount its reality. The other field with a suggestive radial profile is that of SDSS J1508+3328 (obsid 10317), which similarly shows an apparent weak diffuse emission region at 6.8'' W of the mean QSO position, with  $14 \pm 4$  net (0.5-2 keV) counts. There is no other such source apparent in the field. These weak excesses may represent the emission from nearby galaxies that fall individually below the detection level, or from a weak ICM

The ACIS image of SDSS J0813+5416 (obsid 10313) shows signs in the smoothed image of extended emission that could be more filamentary in shape, and so would not register as a significant decrease in a radial profile plot. The emission appears to extend about 80'' from SE to NW. Excluding the QSO regions, and using elliptical source and background apertures (of about 0.7 and sq. arcmin area, respectively), we tally  $64 \pm 12$  net source counts. There are no obvious optical counterparts that might be galaxies associated with a cluster merger or cosmological filament. Assuming a Raymond-Smith plasma with  $T = 2$  keV and metallicity 0.2 solar, we derive  $f(0.5-2 \text{ keV}) = 7.43 \times 10^{-15} \text{ erg cm}^{-2} \text{ s}^{-1}$ . If at the  $z = 0.779$  redshift of the QSOs, the cluster luminosity is  $2.0 \times 10^{43} \text{ erg s}^{-1}$ .

#### 4. Optical Imaging

To look for local galaxy overdensities, and to study deeper imaging of the quasars themselves in a search for signs of merger activity, we obtained observations of six binary QSOs at Kitt Peak National Observatory (KPNO) using the 4m Mayall telescope on the nights of 2009 March 17-19. All images were acquired utilizing the MOSAIC 8K camera ( $8192 \times 8192$  pixels;  $0.26'' \text{ pixel}^{-1}$ ) in one or more filters using the  $r'$ ,  $i'$ , and  $z'$  bandpasses. Integration times ranged from 900 to 9000 s, depending on the filter and the redshift of our binary quasar pair. The seeing varied during the observing run from 0.77'' to 1.69'' (FWHM), as measured from the combined frames.

---

<sup>2</sup>Since SDSS J1606+2900B was not detected by Chandra, we simply use its optical position from SDSS.

Image reduction was conducted using the `mscred` package within the Image Reduction and Analysis Facility (IRAF)<sup>3</sup> environment. Processing of the raw images involved the standard procedure of bias correction and flat-fielding using dome flats and deep sky exposures. After initial processing, individual images were astrometrically corrected and median combined to yield a higher S/N image.

Object detection and photometry was conducted using SExtractor (Bertin & Arnouts 1996) via the ChaMP image reduction pipeline (Green et al. 2004). Since all images were acquired during nonphotometric sky conditions, instrumental magnitudes were transformed to the standard system by calibrating to overlapping SDSS DR7 data using dereddened magnitudes.<sup>4</sup>

With optical imaging of adequate depth, we can detect an overdensity of galaxies photometrically because early-type galaxies at a given redshift have a narrow range of colors which form a cluster “red-sequence” (Gladders & Yee 2000) in their color-magnitude diagram (CMD). In the neighborhood of a QSO pair, the most convincing optical cluster detection would have a large number of optical galaxies clustering at small distances from the QSO pair center, and those galaxies would have well-measured colors clustering at small distances from a single locus in the CMD. We therefore define a distance- and error-weighted color mean (DWCM), given by  $DWCM = \sum \frac{(r-i)_j}{\sigma_j^2} / \sum \frac{1}{\sigma_j^2}$ , where  $\sigma_j^2 = \sigma_{(r-i)_j}^2 + R_j^2$ , and  $R$  is the projected distance from the location center in units of Mpc at the QSO redshift. Thus a bright galaxy with a small color error could contribute as much to the DWCM as a fainter galaxy closer to the center point. With the 1 Mpc scaling, a 250 kpc projected galaxy distance and a typical color error of 0.25 contribute about equally to the weighting. Using the same DWCM calculation for any number of randomly-chosen locations in the same large-field optical image of our quasar field allows us to quantify the significance of the DWCM measured around our QSO pairs, in a way that naturally accounts for the characteristics of the relevant imaging such as depth and image FWHM.

Using unsaturated objects that are unlikely to be point sources, and including only those objects that are brighter than the 50% completeness limit for point sources, we calculate DWCM for 1000 random positions for each of our five quasar pairs with two-filter photometry. We find that there are no significant galaxy density enhancements of the color and magnitudes expected for early-type galaxies at the redshift of our QSO pairs. In Fig-

---

<sup>3</sup>IRAF is distributed by the National Optical Astronomy Observatory, which is operated by the Association of Universities for Research in Astronomy, Inc., under the cooperative agreement with the National Science Foundation.

<sup>4</sup>We compare SDSS `model_Mag` to SExtractor `MAG_AUTO` values.

ure 1 we show a histogram distribution of the weighted mean color ( $i - z$ ) calculated using the DWCM prescription for SDSS J0740. The 1000 DWCM measurements made at random locations are given by the histogram bars, while the DWCM at the position of the quasar pair is depicted by the dashed line. Adopting the red sequence models of Kodama & Arimoto (1997) transformed to the SDSS filters (T. Kodama 2004, private communications), we also plot the expected location of the galaxy red sequence at  $m^*$  based on the redshift of the quasar pair ( $i - z = 1.05$ ; solid vertical line).

If the DWCM at the QSO position was appropriate for the red sequence color expected at the pair redshift, and the red sequence scatter were small, this could be especially convincing evidence for a physical galaxy cluster. To estimate the prominence of the red sequence, we calculate the variance in DWCM and compare the results for our set of random locations with results for the location of the quasar pair. In Figure 1 a contour plot of DWCM versus variance for the SDSS J0740 field is presented, with the value measured at the location of the quasar pair denoted by the asterisk at the 50% contour level. For our five QSO pairs with deep NOAO imaging, there is no evidence for a significantly lower value of the variance of DWCM at the position of our QSO pairs compared to random locations in the quasar fields.

## 5. Near Infrared Imaging

To search for extended host galaxy emission and/or morphological signs of mergers or interactions, we proposed near-IR imaging to optimize the contrast between the relatively blue quasar point source emission and the stellar light from the host galaxies. We were awarded 2 nights to image binary QSOs on Mt Hopkins using the SAO Wide-field InfraRed Camera (SWIRC) on the 6.5m MMT. SWIRC has  $2048 \times 2048$  pixels spanning a  $\sim 5.12'$  field of view with  $0.15''$  pixels. We observed 9 pairs in  $J$  ( $1.2\mu\text{m}$ ) band on the nights of 25 and 26 March 2010 and obtained between  $6 \times 90$  sec and  $33 \times 90$  sec dithered images. We used the SWIRC pipeline to scale and subtract dark images and remove sky background from all the images. The sky image per object frame was created using SExtractor (Bertin & Arnouts 1996). In the  $5.12' \times 5.12'$  field-of-view, each object frame contained at least three stars from the Two Micron All Sky Survey (2MASS) point source catalog (Cutri et al. 2003; Skrutskie et al. 2006), which we used to calibrate the astrometry of each frame and to determine the flux zeropoint, with the magnitude conversions of Rudnick et al. (2001). Based on the turnover in the magnitude range, for our shallower field, a typical exposure of 540 sec results in a limiting magnitude of 18.7 while for our deeper fields with exposure time of 2970 sec turnover magnitude is 20.3. We then used the `imwcs` software in the WCSTools package

(Mink, 1997) to derive sky coordinates. We examined the distribution of FWHM for all images contributing to a given QSO field, exclude any outliers and then stack all the images of a QSO field using the IRAF imcombine task by averaging together with a  $1\sigma$ -clip into stacked science frames of all astrometrically corrected, sky-subtracted images. Small portion of the SWIRC field of view, especially the edges of each image, were disregarded due to significant contamination from CCD artefacts. Each of our stacked images contains between 80 and 120 objects consistent with previous J-band surveys of the same depth (Saracco et al. 2001; Ryan et al. 2008). Seeing at the wavefront sensor varied from 0.7 to 1.1", yielding a typical median FWHM of 1.25" on our stacked images.

For a total of four out of seven pairs in our sample (8 QSOs) SWIRC photometry was obtained. Near-infrared properties are given in Table 3. None of our SWIRC sources has 2MASS *J*-band counterparts, but we find excellent agreement between SWIRC and UKIDSS for the four QSOs with public UKIDSS photometry. We detect point sources for all QSOs, but no evidence of extended emission. Even SDSS J1254+0846, a merger with strong tidal tails detected in the optical bands (Green et al. 2010), shows no SWIRC evidence for the tails.

## 6. Comparison to Single Quasars

The X-ray to optical luminosity ratio is often parameterized by the X-ray-to-optical spectral slope  $\alpha_{\text{ox}}$ <sup>5</sup>. X-rays in quasars become weaker relative to optical emission as luminosity increases, and the 14 QSOs in our sample appear to fall along the expected trends (Steffen et al. 2006; Green et al. 2009). Statistical tests have shown that the correlation is weaker with redshift, so that the  $\alpha_{\text{ox}}(L)$  relationship is not a secondary effect of quasar evolution combined with the strong  $L - z$  trends of flux-limited quasar samples.

\*\*\*\* Do These binary QSO pairs confirm that the observed  $\alpha_{\text{ox}}$  trend with luminosity in quasars is followed even by quasars at the same epoch and in the same large-scale environment.

Our small binary QSO sample has mean (median) redshift  $0.72 \pm 0.18$  (0.77). An excellent control sample is available already through the PI's leadership of the Chandra Multiwavelength Project (ChAMP): we have matched 1175 SDSS QSOs from DR5 (Weinstein et al. 2004), to Chandra serendipitous X-ray sources measured in 323 X-ray images from Cycles 1–6. To form a fair, high quality comparison sample, we limit the ChAMP QSOs to

---

<sup>5</sup> $\alpha_{\text{ox}}$  is the slope of a hypothetical power-law from 2500 Å to 2 keV i.e.,  $\alpha_{\text{ox}} = 0.3838 \log(l_{2500 \text{ \AA}} / l_{2 \text{ keV}})$

those at  $z < 1.2$ , with exposure times  $>4$  ksec, and off-axis angles  $\theta < 12'$ . This yields a control sample of 265 isolated QSOs, with mean (median) redshift  $0.74 \pm 0.32$  (0.79), and a cumulative Chandra exposure of  $\sim 7.7$  Msec. The sample includes 70 QSO candidates (26%) with only photometric redshifts. The additional criterion of X-ray detection means that 98% of these candidates are indeed QSOs. Note that the parent SDSS QSOs were selected optically using *exactly the same approach as that used by Myers et al. (2008) to target binary quasars*. However, since we specifically targeted the binary QSOs with Chandra, their X-ray data is of somewhat higher quality (all on-axis, with a mean of 570 X-ray counts) compared to the control sample (183 counts in the mean). We find no significant difference in any of the measured ensemble properties. Comparing power-law fits, the mean (median)  $\Gamma$  is  $2.14 \pm 0.30$  (2.11) for the binary QSOs, and  $1.96 \pm 0.61$  (2.01) for the comparison sample. The mean (median)  $\alpha_{\text{ox}}$  is  $1.60 \pm 0.21$  (1.59) for the binary QSOs, and  $1.57 \pm 0.16$  (1.57) for the comparison sample.

### 6.1. Comparing $\alpha_{\text{ox}}$

Figure 2 shows  $\alpha_{\text{ox}}$  vs. optical 2500Å log luminosity for the binary QSOs (black diamonds), with pair members linked by black lines. The comparison sample of 265  $z < 1.2$  SDSS QSOs with Chandra detections from (Green et al. 2009) is also plotted, for which red triangles indicate spectroscopic redshifts, and blue circles show radio-loud objects. Binary QSO constituents appear to follow quite well in general the rather noisy well-known trend of  $\alpha_{\text{ox}}$  with optical luminosity (Green et al. 2009; Steffen et al. 2006). Only one QSO, SDSS J160602.81+290048.7 falls well away from the  $\alpha_{\text{ox}}(l_{2500\text{\AA}})$  trend, with  $\alpha_{\text{ox}} = 2.2$  at  $\log l_{2500\text{\AA}} = 30.39$ . This QSO is unusually faint in the X-ray band, and so may be a low redshift broad absorption line quasar (BALQSO). The vast majority of recognized BALQSOs in the SDSS are above redshift 1.6 because only then does the CIV absorption enter the spectroscopic bandpass.<sup>6</sup> In most cases, BALQSOs are X-ray weak due to large warm (ionized) absorbing columns (Green et al. 2001; Gallagher et al. 2006). BALQSOs tend to have narrow H $\beta$  broad line components, weak [OIII] lines, strong optical Fe II emission, and be radio quiet, all of which are apparent in this object’s SDSS spectrum.

If our systems genuinely reflect pairs at an unusual merging stage, perhaps being ignited or exacerbated by an ongoing merger, we might expect to see differences in the properties of the AGN involved in the merger as compared to a random selection of quasars. Simple

---

<sup>6</sup>A much smaller number of the rare low-ionization BALQSOs (with BALs just blueward of MgII) are found at lower redshifts.

statistics where this might be manifest include  $\alpha_{\text{ox}}$  and  $l_{2500\text{Å}}^{\circ}$ . In particular, if one of the nuclei in our pairs is being particularly affected by the merger, we might expect differences between the relative values of  $\alpha_{\text{ox}}$  and  $l_{2500\text{Å}}^{\circ}$  for each component of the pair.

To test this, we derive the differences between  $\alpha_{\text{ox}}$  for each component of each pair, which we denote  $\Delta\alpha_{\text{ox}}$  and the differences between  $l_{2500\text{Å}}^{\circ}$  for each component of each pair which we denote  $\Delta l_{2500\text{Å}}^{\circ}$ . As neither component of our pair is known to be special, we adopt a one-tailed distribution and only allow these differences to be positive in value. We establish the background expectation for the relationship between  $\Delta\alpha_{\text{ox}}$  and  $\Delta l_{2500\text{Å}}^{\circ}$  by selecting 35000 pairs at random from the 264 SDSS DR5 quasars for which we have X-ray data from the ChaMP (note that there are then only 34716 possible unique pairs to sample, so our precision cannot be increased without severely oversampling). In Figure 3 we plot the distribution in density of our 35000 mock pairs in the  $(\Delta\alpha_{\text{ox}}, \Delta l_{2500\text{Å}}^{\circ})$  plane compared to the 7 data points.

It is clear from Figure 3 that most of the pairs are not unusual as compared to background expectation. One of the data pairs is near the extreme of the distribution, with only 7% of mock pairs having similarly extreme values of  $(\Delta\alpha_{\text{ox}}, \Delta l_{2500\text{Å}}^{\circ})$ . However, as we are considering 7 pairs, a result at the 7% probability level is not unusual—indeed it should be expected. We demonstrate this further in the right-hand panel of Figure 3, for which we draw 5000 sets of 7 pairs at random from our 34716 mock pairs and plot the contour (from Figure 3, i.e. the 7% quoted in this paragraph) of the least likely pair in the distributions of 7 mock pairs. The histogram in Figure 3 demonstrates that most random sets of 7 pairs have one pair with a probability at the 7% level. Our data are therefore not unusual in the  $(\Delta\alpha_{\text{ox}}, \Delta l_{2500\text{Å}}^{\circ})$  plane, suggesting that either these values are not unusual for activated nuclei in ongoing mergers, or that we are not seeing a set of 7 ongoing mergers on the data.

Although we detect no substantial differences between the SEDs *or* environments of binary and isolated quasars at these redshifts, we have nevertheless observed a unique sample of 14 luminous quasars exquisitely paired in redshift, optical properties<sup>7</sup> and environment. Removing these latter variables also relieves the usual nagging caveats in comparisons e.g., of  $M_{\text{BH}}$ ,  $L/L_{\text{Edd}}$ , and of two persistently unexplained luminosity *anti*-correlations, the Baldwin Effect ( $W_{\lambda}^{\text{em}}$ ; Baldwin 1977; Green et al. 2001a), and X-ray brightness ( $\alpha_{\text{ox}}$ ; Green et al. 1995; Steffen et al. 2006; Tang et al. 2007).

We can also correlate the SEDs and  $L_{\text{Bol}}$  with binary characteristics like  $R_p$  and  $\Delta v$  – do smaller separations and/or lower velocities result in luminous, high column systems?

---

<sup>7</sup>The largest mag difference between A and B in this sample is  $\sim 2.3$  mag.

## 7. Spectral Energy Distributions

To characterise the SEDs, estimate bolometric luminosities and check for the presence of starburst activity in all QSO pairs in our sample, the near-infrared, optical and X-ray photometric data, described above, are fitted using a library of 12 templates: a radio-quiet Type 1 quasar, a luminosity-dependent radio-quiet Type 1 quasar, two Type-2 Seyferts, four starburst and four composite templates (Ruiz et al. 2010). We fitted all SEDs by using the  $\chi^2$  minimization technique of Ruiz et al (2007; 2010) which benefits from its ability to include X-ray data in the fitting. Existing optical spectroscopy for all our sources removes the uncertainty of using photometric redshifts for the SED fitting and provides a direct testbed for the accuracy of the fitting method. Broad-band SEDs for all 14 sources are given in Figures 4 and ???. Table 4 gives the different parameters of our best SED fits.

In all 14 cases, either a radio quiet Type-1 QSO (Richards et al. 2006 for  $\nu > 10^{12}$  Hz and Elvis et al. 1994 for  $\nu < 10^{12}$  Hz) or an AGN luminosity dependent template (Hopkins et al. 2007) is needed to fit the photometry, consistent with the fact that all our sources are spectroscopically identified broad line QSOs. Nonetheless, in 5 out of 7 pairs, at least one of the pair components, 8 out of 14 sources in total, the template solution which best-fits our near-infrared to X-ray photometry requires an additional starburst component.

When the AGN and/or starburst component contribution is estimated over the  $10^{14}$  -  $10^{18}$  Hz wavelength range, where we have available photometry, the luminosity of all 14 sources appears to originate mainly from an AGN component ( $>55\%$ ). However, in the case of the 8 sources that require a starburst component, star-formation activity contributes at least 20% of the luminosity emitted between  $10^{14} - 10^{18}$  Hz. When we integrate luminosity over the entire radio to X-ray wavelength range, starburst activity becomes the dominant component ( $>90\%$ ) in 6 cases, which may be indicative of intense star-formation events in their hosts. We warn, however, that the bulk of the starburst template contribution comes from wavelengths longer than we have data (far-IR to radio).

The predicted SED fits suggest that the majority of the QSO pairs in our sample (5 of 7) have ongoing powerful starburst events. Interestingly, the one one pair, SDSS J1254+0846 (Green et al. 2010), that is known to inhabit, does not require a significant contribution from star formation. Previous studies of X-ray- (Trichas et al. 2009) and spectroscopically- (Lutz et al. 2008; Trichas et al. 2010; Kalfountzou et al. 2010; Symeonidis et al 2010) selected QSOs with far-infrared detections have shown that the vast majority of these sources are composite objects with very strong ongoing starburst events. Although, these studies were focused on the brightest and rarest examples, subsequent studies of submillimeter detected Type-1 QSOs (Lutz et al. 2010; Hatziminaoglou et al. 2010) have made clear that the submm colors of Type-1 QSOs are similar to those of star-forming galaxies indicating the

presence of star-formation activity in all AGN. All these results are consistent with Hopkins et al. (2005) merger model and in this case the tendency we see in our QSO pairs is expected. On the other hand in the local Universe, all black hole accretion as detected by hard X-rays is strongly disassociated with star formation implying that there is a fundamental anti-correlation between the two that is not a selection effect (Schawinski et al. 2009). In the latter case, the prediction of starburst activity in the majority of the QSO pairs in our sample has strong implications for the dynamics of these merger systems that needs to be further investigated.

It would be of great interest to test whether this tendency is statistically different to isolated QSOs and in a subsequent paper, we are planning to utilize the large number of ChaMP spectroscopically identified isolated QSOs in order to compare their SEDs to a much larger sample of spectroscopically identified QSO pairs (e.g. Myers et al. 2008). Inclusion of Spitzer, Herschel and ALMA bands would greatly improve our understanding of the infrared properties of these systems and would directly provide evidence for the presence of star-formation activity predicted by our SEDs.

## 8. Conclusions

The fraction of galaxies hosting actively accreting supermassive black holes (SMBHs) evolves with cosmic time (Shen et al. 2010a; Haggard et al. 2010; Martini et al. 2009; Shi et al. 2008) and is likewise affected by environment (e.g., Strand et al. 2008). This fraction convolves two seemingly distinct probabilities - first, that a SMBH has formed and second, that it is actively accreting. However, the former (the black hole occupation fraction) is just an integration over the black hole mass function, which is itself the accretion rate in galaxies integrated over cosmic time. Therefore, the active fraction can be viewed as a snapshot of the accretion history, which depends strongly on both the host galaxy characteristics and its environment. If the accretion history were steady over cosmic time, then the active fraction could be thought of as a single AGN duty cycle (Schawinski et al. 2010).

Across cosmic time, more massive galaxies host active nuclei more frequently (Shi et al. 2008). In the local universe, it has been found that the AGN fraction depends on the host stellar mass (e.g., Kauffmann et al. 2003a; Gallo et al. 2008; Decarli et al. 2007; Sivakoff et al. 2008), host Hubble type (Ho et al. 1997), and SMBH mass (Heckman et al. 2004; Greene & Ho 2007b). Note that these three parameters are roughly correlated with each other. In general, the fraction harboring active nuclei is lower for lower mass systems locally.

However, the integrated impact of such powerful activity in the nuclei of galaxies may

far exceed their numbers, affecting the origin, growth, and evolution of massive galaxies.

Support for this work was provided by the National Aeronautics and Space Administration through Chandra Award Number GO9-0114A issued by the Chandra X-ray Observatory Center, which is operated by the Smithsonian Astrophysical Observatory for and on behalf of the National Aeronautics Space Administration under contract NAS8-03060. Discovery optical images were obtained at Kitt Peak National Observatory, National Optical Astronomy Observatory, which is operated by the Association of Universities for Research in Astronomy (AURA) under cooperative agreement with the National Science Foundation. This research has made use of data obtained from the Chandra Data Archive and software provided by the Chandra X-ray Center (CXC) in the application packages CIAO, and Sherpa. This paper has used data from the SDSS archive. Funding for the SDSS and SDSS-II has been provided by the Alfred P. Sloan Foundation, the Participating Institutions, the NSF, the US Department of Energy, the National Aeronautics and Space Administration (NASA), the Japanese Monbukagakusho, the Max Planck Society, and the Higher Education Funding Council for England. The SDSS website is at <http://www.sdss.org/>.

Thanks to Doug Mink and Bill Wyatt (SAO) for help with the SWIRC pipeline.

*Facilities:* Mayall () Magellan:Baade () CXO (),

Chandra ObsId 10315

### Appendix: Explicit X-ray Flux and Luminosity Calculations

We often assume the monochromatic flux density for an underlying intrinsic power-law to have form  $f \propto \nu^\alpha$ , where  $f$  is the monochromatic flux (e.g., in  $\text{erg cm}^{-2} \text{s}^{-1} \text{Hz}^{-1}$ ) and  $\nu$  is the power-law frequency index. For X-rays, the photon index  $\Gamma$  is more commonly used, where  $\alpha = (1 - \Gamma)$ .

We fit an X-ray power-law spectral model

$$N(E) = N(E_0) \left( \frac{E}{E_0} \right)^{(1-\Gamma)} \exp[-N_H^{Gal} \sigma(E) - N_H^z \sigma(E(1+z))]$$

to the X-ray counts as a function of energy, where  $N(E_0)$  is the normalization in photons  $\text{cm}^{-2} \text{sec}^{-1} \text{keV}^{-1}$  at a chosen reference energy  $E_0$ ,  $\Gamma$  is the photon index, and  $\sigma(E)$  is the absorption cross-section. We fix  $N_H^{Gal}$  at the appropriate Galactic neutral absorbing column, and allow for an intrinsic absorber with neutral column  $N_H^z$  at the source redshift.

The X-ray monochromatic energy flux without the effects of absorption is

$$f(E) = E N(E) = E N(E_0) \left( \frac{E}{E_0} \right)^{(1-\Gamma)}$$

in  $\text{keV cm}^{-2} \text{sec}^{-1} \text{keV}^{-1}$ . Then, since  $f(E_0) = E_0 N(E_0)$ , we can express the monochromatic energy flux as

$$f(E) = f(E_0) \left( \frac{E}{E_0} \right)^{(1-\Gamma)},$$

To obtain the more standard units of  $\text{erg cm}^{-2} \text{sec}^{-1} \text{Hz}^{-1}$ , multiply by  $6.629 \times 10^{-27}$  (from conversion factors  $1.602 \times 10^{-9} \text{erg/keV}$  and  $\text{Hz}^{-1} = h \text{keV}^{-1}$  where  $h = 4.138 \times 10^{-18} \text{keV/Hz}$ ).

The integrated flux observed between energies  $E_1$  and  $E_2$  is

$$F = \int_{E_1}^{E_2} f(E) dE = \frac{f(E_0)}{E_0^{(1-\Gamma)}} \frac{[E_2^{(2-\Gamma)} - E_1^{(2-\Gamma)}]}{(2-\Gamma)} = \frac{N(E_0)}{E_0^{-\Gamma}} \frac{[E_2^{(2-\Gamma)} - E_1^{(2-\Gamma)}]}{(2-\Gamma)}$$

If  $F$  above is in units of  $\text{keV cm}^{-2} \text{sec}^{-1}$ , multiplying by  $1.602 \times 10^{-9}$  yields observed broadband flux in  $\text{erg cm}^{-2} \text{sec}^{-1}$ .

Note that as  $\Gamma \rightarrow 2$ , via L'Hospital's rule  $F \rightarrow \frac{N(E_0)}{E_0^{-\Gamma}} \ln(E_2/E_1)$ . Note also that to convert from one broadband flux (or luminosity) to another

$$\frac{F(E_3 - E_4)}{F(E_1 - E_2)} = \frac{[E_4^{(2-\Gamma)} - E_3^{(2-\Gamma)}]}{[E_2^{(2-\Gamma)} - E_1^{(2-\Gamma)}]}$$

Due to the redshift, the measured spectral flux  $f_\nu$  is related to the spectral rest-frame luminosity  $L_{\nu'}$ , where  $\nu' = (1+z)\nu$ , as

$$f_\nu = \frac{(1+z) L_{\nu'}}{4 \pi d_L^2}$$

The factor of  $(1+z)$  accounts for the fact that the flux and luminosity are not bolometric, but are densities per unit frequency. (The factor would appear in the denominator if the expression related flux and luminosity densities per unit wavelength.)

The monochromatic luminosity is therefore

$$L_{\nu'} = \frac{4 \pi d_L^2}{(1+z)} f_\nu = \frac{4 \pi d_L^2}{(1+z)} f_{\nu'} \left( \frac{f_\nu}{f_{\nu'}} \right)$$

but since  $f_\nu \propto \nu^\alpha$  and  $\alpha = (1-\Gamma)$ ,

$$\left( \frac{f_\nu}{f_{\nu'}} \right) = \left( \frac{\nu}{\nu'} \right)^{(1-\Gamma)}$$

so that

$$L_{\nu'} = 4 \pi d_L^2 (1 + z)^{(\Gamma-2)} f_{\nu'}$$

in  $\text{erg sec}^{-1} \text{Hz}^{-1}$ . In this way, the flux measured at  $\nu'$  in the observed frame yields the monochromatic luminosity  $L_{\nu'}$  in the rest frame.

The broadband luminosity in  $\text{erg sec}^{-1}$  is therefore

$$L_X = \int_{\nu_1}^{\nu_2} L(\nu) d\nu = 4 \pi d_L^2 (1 + z)^{(\Gamma-2)} \int_{\nu_1}^{\nu_2} f(\nu) d\nu.$$

Then, since

$$\begin{aligned} \int_{\nu_1}^{\nu_2} f(\nu) d\nu &= f(\nu_0) \int_{\nu_1}^{\nu_2} \left(\frac{\nu}{\nu_0}\right)^{(1-\Gamma)} d\nu, \\ &= \frac{f(\nu_0)}{\nu_0^{(1-\Gamma)}} \left[ \frac{\nu^{(2-\Gamma)}}{(2-\Gamma)} \right]_{\nu_1}^{\nu_2} = \frac{f(\nu_0)}{\nu_0^{(1-\Gamma)}} \frac{[\nu_2^{(2-\Gamma)} - \nu_1^{(2-\Gamma)}]}{(2-\Gamma)} \end{aligned}$$

we get

$$L_X = 4 \pi d_L^2 (1 + z)^{(\Gamma-2)} \frac{f(\nu_0)}{\nu_0^{(1-\Gamma)}} \left[ \frac{\nu_2^{(2-\Gamma)} - \nu_1^{(2-\Gamma)}}{(2-\Gamma)} \right]$$

where the final term is convenient for L'Hospital's rule. Perhaps more intuitively, we can write

$$L_X = 4 \pi d_L^2 (1 + z)^{(\Gamma-2)} \left[ \frac{\nu_2 f(\nu_2) - \nu_1 f(\nu_1)}{(2-\Gamma)} \right]$$

To substitute  $E$  in keV for frequencies above, just multiply by  $2.41666 \times 10^{17} \text{ Hz/keV}$ .

## REFERENCES

- Aldcroft, T. L., & Green, P. J. 2003, ApJ, 592, 710
- Aoki, K., Kawaguchi, T., & Ohta, K. 2005, ApJ, 618, 601
- Bahcall, J. N., Kirhakos, S., Saxe, D. H., & Schneider, D. P. 1997, ApJ, 479, 642
- Barkhouse, W. A., et al. 2006, ApJ, 645, 955
- , Barr, J. M., et al. 2003, MNRAS, 346, 229
- Begelman, M. C., Blandford, R. D., & Rees, M. J. 1980, Nature, 287, 307
- Bennert, N., Falcke, H., Schulz, H., Wilson, A. S., & Wills, B. J. 2002, ApJ, 574, L105

- Bennert, N., Canalizo, G., Jungwiert, B., Stockton, A., Schweizer, F., Peng, C. Y., & Lacy, M. 2008, *ApJ*, 677, 846
- Bertin, E. 2006, *SWarp ver. 2.16 Users Guide* (Paris: Terapix), <http://terapix.iap.fr/IMG/pdf/swarp.pdf>
- Bertin, E., & Arnouts, S. 1996, *A&AS*, 117, 393
- Bianchi, S., Chiaberge, M., Piconcelli, E., Guainazzi, M., & Matt, G. 2008, *MNRAS*, 386, 105
- Bogdanović, T., Eracleous, M., & Sigurdsson, S. 2009, *ApJ*, 697, 288
- Boroson, T. A., & Green, R. F. 1992, *ApJS*, 80, 109
- Boroson, T.A. & Lauer, T.R. 2009, *Nature*, 458, 53
- Burud, I., et al. 2002a, *A&Ap*, 383, 71
- Burud, I., et al. 2002, *A&Ap*, 391, 481
- Cash, W. 1979, *ApJ*, 228, 939
- Cheung, C. C. 2007, *AJ*, 133, 2097
- Chornock, R., et al. 2010, *ApJ*, 709, L39
- Civano, F., et al. 2010, *ApJ*, 717, 209
- Comerford, J. M., et al. 2009a, *ApJ*, 698, 956
- Condon, J. J., Cotton, W. D., Greisen, E. W., Yin, Q. F., Perley, R. A., Taylor, G. B., & Broderick, J. J. 1998, *AJ*, 115, 1693
- Cox, T. J., Dutta, S. N., Di Matteo, T., Hernquist, L., Hopkins, P. F., Robertson, B., & Springel, V. 2006, *ApJ*, 650, 791
- Croom, S. M. et al. 2005, *MNRAS*, 356, 415
- Cui, J., et al. 2001, *AJ*, 122, 63
- de Vaucouleurs, G. 1948, *Ann. d’Astrophys.*, 11, 247
- Dickey, J. M., & Lockman, F. J. 1990, *Annu. Rev. Astron. Astrophys.*, 28, 215
- Djorgovski, S. G., et al. 1987, *ApJ*, 321, L17

- Djorgovski, S. 1991, *The Space Distribution of Quasars*, 21, 349
- Donoso, E., Li, C., Kauffmann, G., Best, P. N., & Heckman, T. M. 2010, *MNRAS*, 407, 1078
- Dunlop, J. S., McLure, R. J., Kukula, M. J., Baum, S. A., ODea, C. P., & Hughes, D. H. 2003, *MNRAS*, 340, 1095
- Elvis, M., et al., 1994, *ApJS*, 95, 1
- Escala, A., Larson, R. B., Coppi, P. S., & Mardones, D. 2004, *ApJ*, 607, 765
- Ferrarese, L., & Merritt, D. 2000, *ApJ*, 539, L9
- Gallagher, S. C., Brandt, W. N., Chartas, G., Priddey, R., Garmire, G. P., & Sambruna, R. M. 2006, *ApJ*, 644, 709
- Gallagher, S. C., Hines, D. C., Blaylock, M., Priddey, R. S., Brandt, W. N., & Egami, E. E. 2007, *ApJ*, 665, 157
- Gebhardt, K., et al. 2000, *ApJ*, 539, L13
- Gibson, R. R., et al. 2009, *ApJ*, 692, 758
- , G. L., et al. 2004, *ApJ*, 600, 580
- Green, P. J., Aldcroft, T. L., Mathur, S., Wilkes, B. J., & Elvis, M. 2001, *ApJ*, 558, 109
- Green, P. J., et al. 2002, *ApJ*, 571, 721
- Green, P. J., et al. 2004, *ApJS*, 150, 43
- Green, P. J., Infante, L., Lopez, S., Aldcroft, T. L., & Winn, J. N. 2005, *ApJ*, 630, 142
- Green, P. J. 2006, *ApJ*, 644, 733
- Green, P. J. et al. 2009, *ApJ*, 690, 644
- Green, P. J., Myers, A. D., Barkhouse, W. A., Mulchaey, J. S., Bennert, V. N., Cox, T. J., & Aldcroft, T. L. 2010, *ApJ*, 710, 1578
- Gregg, M. D., Becker, R. H., & de Vries, W. 2006, *ApJ*, 641, 210
- Haggard, D., Green, P. J., Anderson, S. F., Constantin, A., Aldcroft, T. L., Kim, D.-W., & Barkhouse, W. A. 2010, *ApJ*, 723, 1447
- Hatziminaoglou, E., et al., 2010, *A&A*, 518, 33

- Hennawi, J. F., et al. 2006, *AJ*, 131, 1
- Hennawi, J. et al. 2010, *ApJ*, 719, 1672
- Hernquist, L. 1989, *Nature*, 340, 687
- Hogg, D. W. 1999, arXiv:astro-ph/9905116
- Hopkins, P., et al., 2005, *ApJ*, 630, 705
- Hopkins, P., et al., 2007a, *ApJ*, 654, 731
- Hopkins, P. F., et al. 2007b, *ApJ*, 662, 110
- Hopkins, P. F., Hernquist, L., Cox, T. J., & Kereš, D. 2008, *ApJS*, 175, 356
- Ivezić, Z., et al. 2002, *AJ*, 124, 2364
- Jonsson, P., Groves, B., & Cox, T. J. 2009, arXiv:0906.2156
- Kaspi, S., Smith, P. S., Netzer, H., Maoz, D., Jannuzi, B. T. & Giveon, U. 2000, *ApJ*, 533, 631
- Kalfountzou, E., et al., 2010, *MNRAS* accepted, astro-ph/1005.4353
- Lutz, D., et al., 2008, *ApJ*, 684, 853
- Lutz, D., et al., 2010, *ApJ*, 712, 1287
- Kaspi, S., Maoz, D., Netzer, H., Peterson, B. M., Vestergard, M. & Jannuzi, B. T. 2005, *ApJ*, 629, 61
- Kauffmann, G. & Haehnelt, M. 2000, *MNRAS*, 311, 576
- Keeton, C. R. 2001, arXiv:astro-ph/0102340
- Kellermann, K. I., Sramek, R. A., Schmidt, M., Green, R. F., & Shaffer, D. B. 1994, *AJ*, 108, 1163
- Kim, M., Ho, L. C., Peng, C. Y., Barth, A. J., & Im, M. 2008a, *ApJS*, 179, 283
- Khochfar, S., & Burkert, A. 2001, *ApJ*, 561, 517
- Kochanek, C. S., Falco, E., Munoz, J. A. 1999, *ApJ*, 510, 590
- Kodama, T., & Arimoto, N. 1997, *A&Ap*, 320, 41

- Komossa, S., et al. 2003, *ApJ*, 582, L15
- Komossa, S., Zhou, H., & Lu, H. 2008a, *ApJL*, 678, L81
- Komossa, S., Xu, D., Zhou, H., Storchi-Bergmann, T., & Binette, L. 2008b, *ApJ*, 680, 926
- Koratkar, A. P. & Gaskell, C. M. 1991, *ApJ*, 370, L61
- Kurtz, M. J., Mink, D. J., Wyatt, W. F., Fabricant, D. G., Torres, G., Kriss, G. A., & Tonry, J. L. 1992, *Astronomical Data Analysis Software and Systems I*, 25, 432
- Laor, A., & Behar, E. 2008, *MNRAS*, 390, 847
- Lauer, T.R. & Boroson, T.A. 2009, *ApJ*, submitted (arXiv:0905.4733)
- Liu, F. K. 2004, *MNRAS*, 347, 1357
- Liu, X., Shen, Y., Strauss, M. A., & Greene, J. E. 2010, *ApJ*, 708, 427
- Madau, P., & Quataert, E. 2004, *ApJ*, 606, L17
- Martini, P., Sivakoff, G. R., & Mulchaey, J. S. 2009, *ApJ*, 701, 66
- Masters, K. L., Springob, C. M., Haynes, M. P., & Giovanelli, R. 2006, *ApJ*, 653, 861
- McLure, R. J., & Dunlop, J. S. 2004, *MNRAS*, 352, 1390
- Merritt, D., & Ekers, R. D. 2002, *Science*, 297, 1310
- Milosavljević, M., & Merritt, D. 2001, *ApJ*, 563, 34
- Milosavljević, M., & Merritt, D. 2003, *The Astrophysics of Gravitational Wave Sources*, 686, 201
- Mink, D. J. 1997, *Astronomical Data Analysis Software and Systems VI*, 125, 249
- Morrison, R, McCammon D. 1983, *ApJ*, 270, 119
- Mortlock, D. J., Webster, R. L., & Francis, P. J. 1999, *MNRAS*, 309, 836
- Montenegro-Montes, F. M., Mack, K.-H., Benn, C. R., Carballo, R., González-Serrano, J. I., Holt, J., & Jiménez-Luján, F. 2009, *Astronomische Nachrichten*, 330, 157
- Motta, V., Mediavilla, E., Muñoz, J. A., & Falco, E. 2004, *ApJ*, 613, 86
- Myers, A. D. et al. 2006, *ApJ*, 638, 622

- Myers, A. D., 2007, *ApJ*, 658, 85
- Myers, A. D., 2007, *ApJ*, 658, 99
- Myers, A. D., Richards, G. T., Brunner, R. J., Schneider, D. P., Strand, N. E., Hall, P. B., Blomquist, J. A., & York, D. G. 2008, *ApJ*, 678, 635
- Oguri, M. et al. 2005, *ApJ*, 622, 106
- Peebles P. J. E., 1993, *Principles of Physical Cosmology*, Princeton University Press, Princeton
- Peng, C. Y., Ho, L. C., Impey, C. D., & Rix, H.-W. 2002, *AJ*, 124, 266
- Perley, R., et al. 2009, *Proceedings of the IEEE*, 97, 1448, arXiv:0909.1585v1
- Perna, R., & Keeton, C. R. 2009, *MNRAS*, 397, 1084
- Peterson, B. M. 1993, *PASP*, 105, 247
- Peterson, B. M., et al. 2004, *ApJ*, 613, 682
- Richards et al. 2006, *ApJS*, 166, 470
- Richards, G. T., et al. 2009, *ApJS*, 180, 67
- Richstone, D., et al. 1998, *Nature*, 395, A14
- Ross, N. P., et al. 2009, *ApJ*, 697, 1634
- Ruiz, A., et al., 2007, *A&A*, 471, 775
- Ruiz, A., Miniutti, G., Panessa, F., & Carrera, F. J. 2010, *A&A*, 515, A99
- Schawinski, K., et al., 2009, *ApJ*, 692, 19
- Schawinski, K., et al. 2010, *ApJ*, 711, 284
- Schmitt, H. R., Pringle, J. E., Clarke, C. J., & Kinney, A. L. 2002, *ApJ*, 575, 150
- Sérsic, J. L. 1968, *Atlas de galaxias australes* (Cordoba, Argentina: Observatorio Astronómico, 1968)
- Shen Y. et al., 2007, *AJ*, 133, 2222

- Shen, Y., Greene, J. E., Strauss, M. A., Richards, G. T., & Schneider, D. P. 2008, *ApJ*, 680, 169
- Shen, Y. 2009, *ApJ*, 704, 89
- Shen, Y., et al. 2010, *ApJ*, 719, 1693
- Shen, Y., Liu, X., Greene, J., & Strauss, M. 2010, arXiv:1011.5246
- Shi, Y., Rieke, G., Donley, J., Cooper, M., Willmer, C., & Kirby, E. 2008, *ApJ*, 688, 794
- Shields, G. A., et al. 2009, *ApJ*, 707, 936
- Sillanpaa, A., Haarala, S., Valtonen, M. J., Sundelius, B., & Byrd, G. G. 1988, *ApJ*, 325, 628
- Silverman, J. D., et al. 2005, *ApJ*, 624, 630
- Sluse, D., Claeskens, J.-F., Hutsemékers, D., & Surdej, J. 2007, *A&Ap*, 468, 885
- Smith, K. L., Shields, G. A., Bonning, E. W., McMullen, C. C., Rosario, D. J., & Salviander, S. 2010, *ApJ*, 716, 866
- Matteo, T., & Hernquist, L. 2005, *MNRAS*, 361, 776
- Springel, V. et al. 2005, *Nature*, 435, 629
- Springel, V. 2009, arXiv:0901.4107
- Steffen, A. T., Strateva, I., Brandt, W. N., Alexander, D. M., Koekemoer, A. M., Lehmer, Strand, N. E., Brunner, R. J., & Myers, A. D. 2008, *ApJ*, 688, 180
- Strateva, I. V., et al. 2003, *AJ*, 126, 1720
- Symeonidis, M., et al., 2010, *MNRAS*, 403, 1474
- Trichas, M., et al., 2009, *MNRAS*, 399, 663
- Trichas, M., et al., 2010, *MNRAS*, 405, 2243
- Tang, S. M., Zhang, S. N., & Hopkins, P. F. 2007, *MNRAS*, 377, 1113
- Tang, S., & Grindlay, J. 2009, *ApJ*, 704, 1189
- Toomre, A., & Toomre, J. 1972, *ApJ*, 178, 623
- Urrutia, T., Lacy, M., & Becker, R. H. 2008, *ApJ*, 674, 80

- Valtonen, M. J., et al. 2009, ApJ, 698, 781
- Vestergaard, M. & Peterson, B. M. 2006, ApJ, 641, 689
- Vivek, M., Srianand, R., Noterdaeme, P., Mohan, V., & Kuriakosde, V. C. 2009, MNRAS, 400, L6
- Volonteri, M., Haardt, F., & Madau, P. 2003, ApJ, 582, 559
- Wandel, A., Peterson, B. M., & Malkan, M. A. 1999, ApJ, 526, 579
- Wang, J.-M., Chen, Y.-M., Hu, C., Mao, W.-M., Zhang, S., & Bian, W.-H. 2009, ApJ, 705, L76
- Weymann, R. J., Morris, S. L., Foltz, C. B., & Hewett, P. C. 1991, ApJ, 373, 23
- White, R. L., Becker, R. H., Helfand, D. J., & Gregg, M. D. 1997, ApJ, 475, 479  
(<http://sundog.stsci.edu/top.html>)
- Wild, V., & Hewett, P. C. 2005, MNRAS, 361, L30
- Wilms, J., Allen, A., & McCray, R. 2000, ApJ, 542, 914
- Wisotzki, L., Koehler, T., Kayser, R., & Reimers, D. 1993, A&Ap, 278, L15
- Wolf, C., et al. 2003, A&Ap, 408, 499
- Wrobel, J. M., & Laor, A. 2009, ApJ, 699, L22
- Wyithe, J. S. B., & Loeb, A. 2003, ApJ, 595, 614
- Wyithe, J. S. B., & Loeb, A. 2002, ApJ, 581, 886
- Wyithe, J. S. B., & Loeb, A. 2005, ApJ, 634, 910
- Xu, D., & Komossa, S. 2009, ApJ, 705, L20
- Yan, R., Newman, J. A., Faber, S. M., Konidakis, N., Koo, D., & Davis, M. 2006, ApJ, 648, 281
- Yuan, W., Siebert, J., & Brinkmann, W. 1998, A&A, 334, 498
- Zezas, A., Ward, M. J., & Murray, S. S. 2003, ApJL, 594, L31

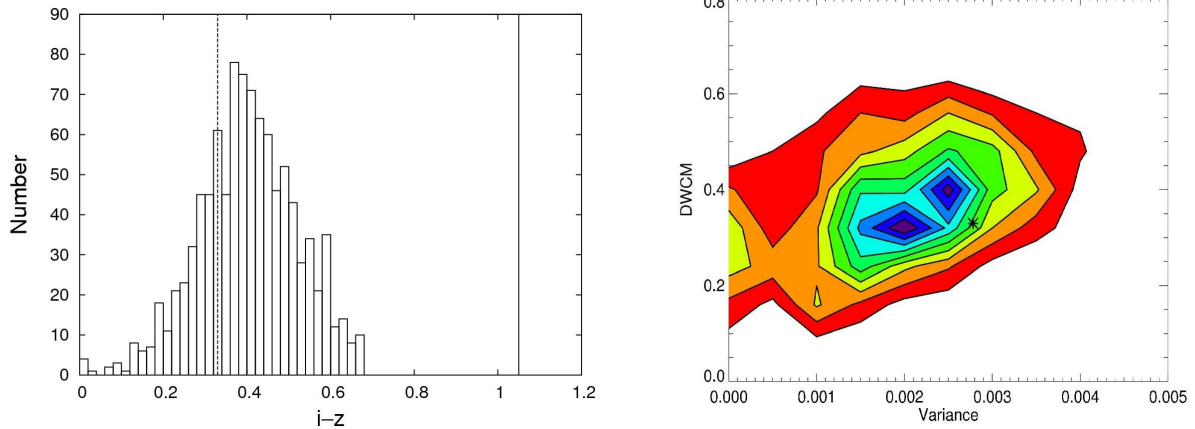


Fig. 1.— Test of optical cluster significance. (LEFT) Histogram distribution of the weighted mean color ( $i - z$ ) calculated using the DWCM prescription for SDSS J0740. The 1000 DWCM measurements made at random locations are given by the histogram bars, while the DWCM at the position of the quasar pair is depicted by the dashed line. The expected location ( $i - z = 1.05$ ) of the galaxy red sequence at  $m^*$  based on the  $z \sim 0.98$  redshift of the quasar pair is shown as a solid vertical line, adopting the red sequence models of Kodama & Arimoto (1997). (RIGHT) Contour plot of DWCM versus its variance for the SDSS J0740 field, with the value measured at the location of the quasar pair denoted by the asterisk at the 50% contour level. There is no evidence for a significant optical cluster of galaxies at any redshift at the position of this QSO pair, compared to random locations in the quasar image field.

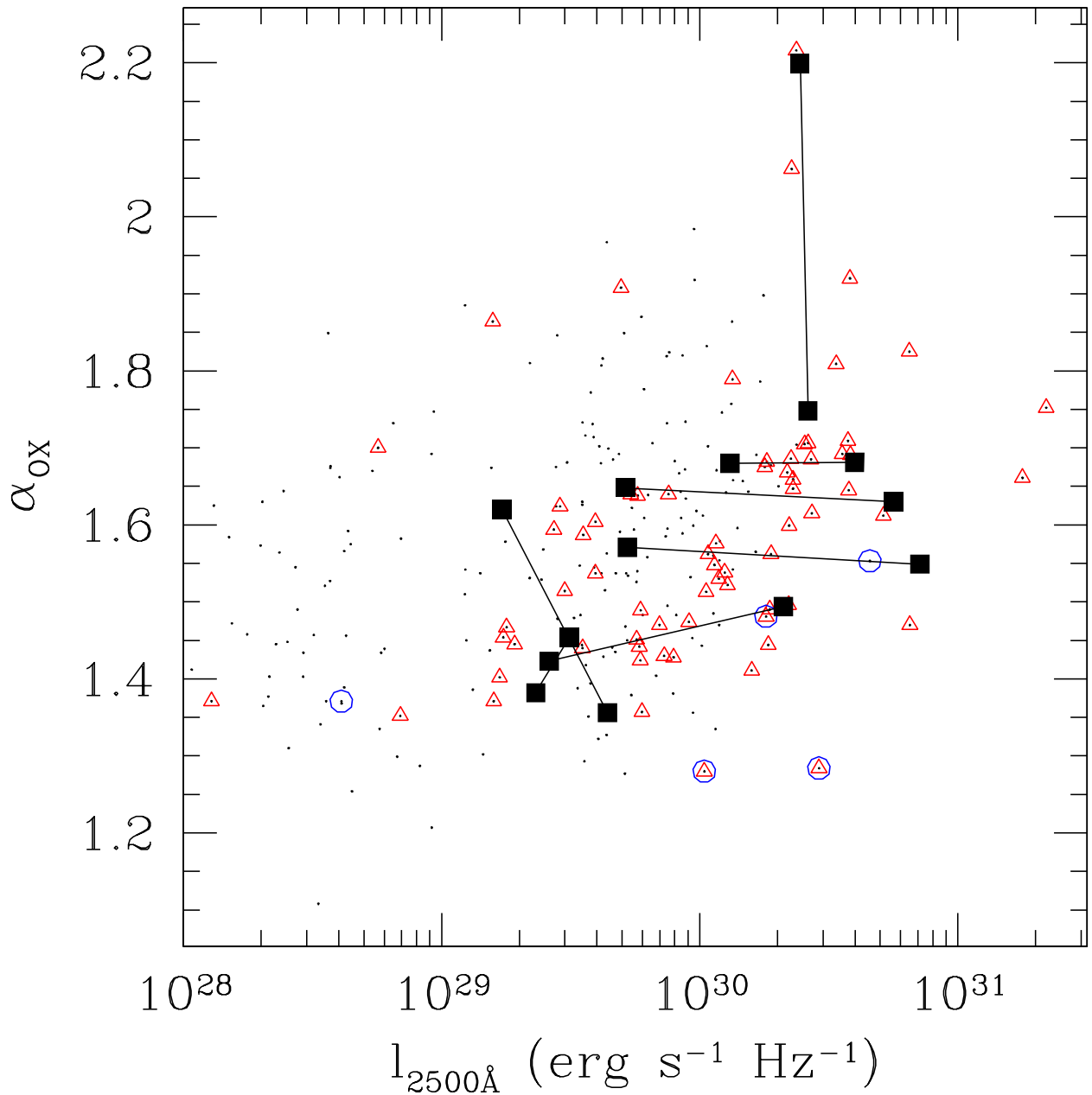


Fig. 2.—  $\alpha_{\text{ox}}$  vs. optical 2500Å log luminosity for the binary QSOs (black diamonds), with pair members linked by black lines. The comparison sample of 265  $z < 1.2$  SDSS QSOs with Chandra detections from Green et al. (2009) is also plotted, for which red triangles indicate spectroscopic redshifts, and blue circles show radio-loud objects.

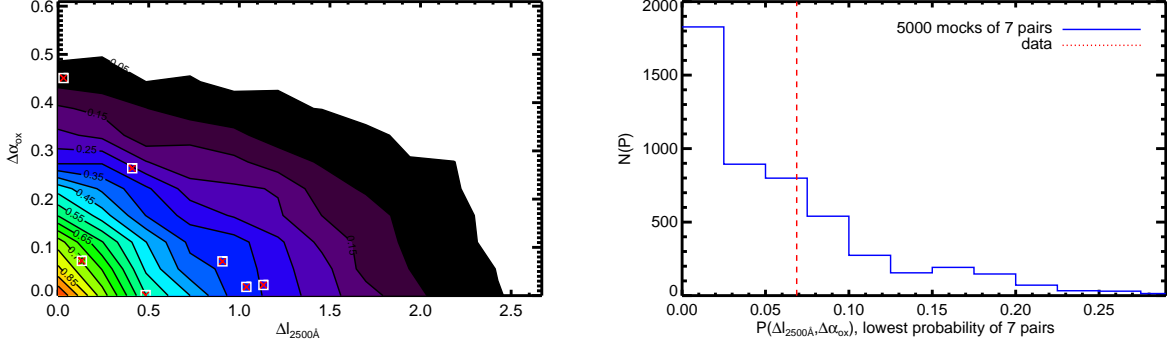


Fig. 3.— LEFT: Distributions of  $\Delta\alpha_{\text{ox}}$ ,  $\Delta l_{2500\text{\AA}}$  for individual quasars and our 7 pairs of close quasars. The contours are the density of 10,000 pairs of quasars drawn at random from the 264 SDSS DR5 quasars in the ChaMP. Points are the 7 genuine pairs of quasars discussed in this paper. The most extreme of the 7 data points has a 7% probability of being drawn at random from the distribution of possible pairs of quasars. RIGHT: As our sample represents drawing 7 pairs of quasars, rather than just one pair, we repeat our experiment but testing instead the most improbable pair drawn at random in 1000 samples of 7 mock pairs. We histogram the value of the contour (i.e. from the right-hand panel) for the most improbable of the 7 mock pairs. The dashed line is for the data.

Table 1. Chandra Close Binary Quasar Sample

| Pair Name       | ObsID | Exposure<br>(sec) | $\theta$ <sup>a</sup><br>(arcsec) | $R_p$ <sup>b</sup><br>(kpc) | Galactic $N_{\text{H}}$ <sup>c</sup><br>( $10^{20} \text{ cm}^{-2}$ ) |
|-----------------|-------|-------------------|-----------------------------------|-----------------------------|---|
| SDSS J0740+2926 | 10312 | 20859             | 2.6                               | 15.0                        | 4.24  |
| SDSS J0813+5416 | 10313 | 30625             | 5.0                               | 26.9                        | 4.21  |
| SDSS J1158+1235 | 10314 | 30827             | 3.6                               | 17.0                        | 2.07  |
| SDSS J1254+0846 | 10315 | 15967             | 3.8                               | 15.4                        | 1.92  |
| SDSS J1418+2441 | 10316 | 29762             | 4.5                               | 21.0                        | 2.00  |
| SDSS J1508+3328 | 10317 | 31317             | 2.9                               | 16.0                        | 1.51  |
| SDSS J1606+2900 | 10318 | 12852             | 3.5                               | 18.4                        | 3.19  |

<sup>a</sup>Separation between QSO components in arcsec.

<sup>b</sup>Proper separation between QSO components in kpc.

<sup>c</sup>Galactic column in units  $10^{20} \text{ cm}^{-2}$  from the NRAO dataset of Dickey & Lockam (1990).

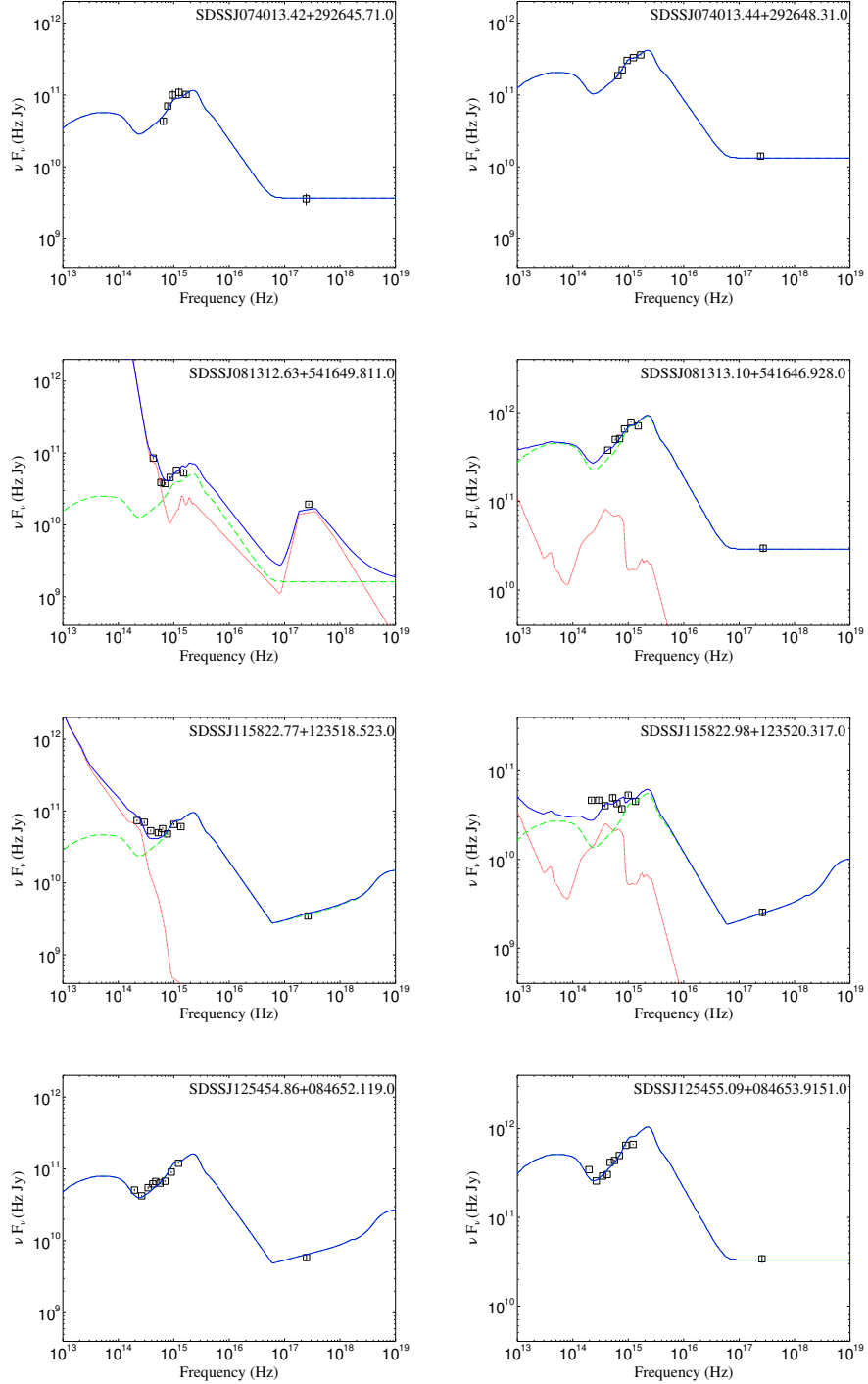


Fig. 4.— Near-infrared to X-ray SEDs (Ruiz et al. 2010) in  $\nu f_\nu$  for all our quasar pairs. Solid blue lines show the total predicted SED. Green and red lines are the corresponding AGN and starburst templates used. Parameters for model fits are given in Table 4.

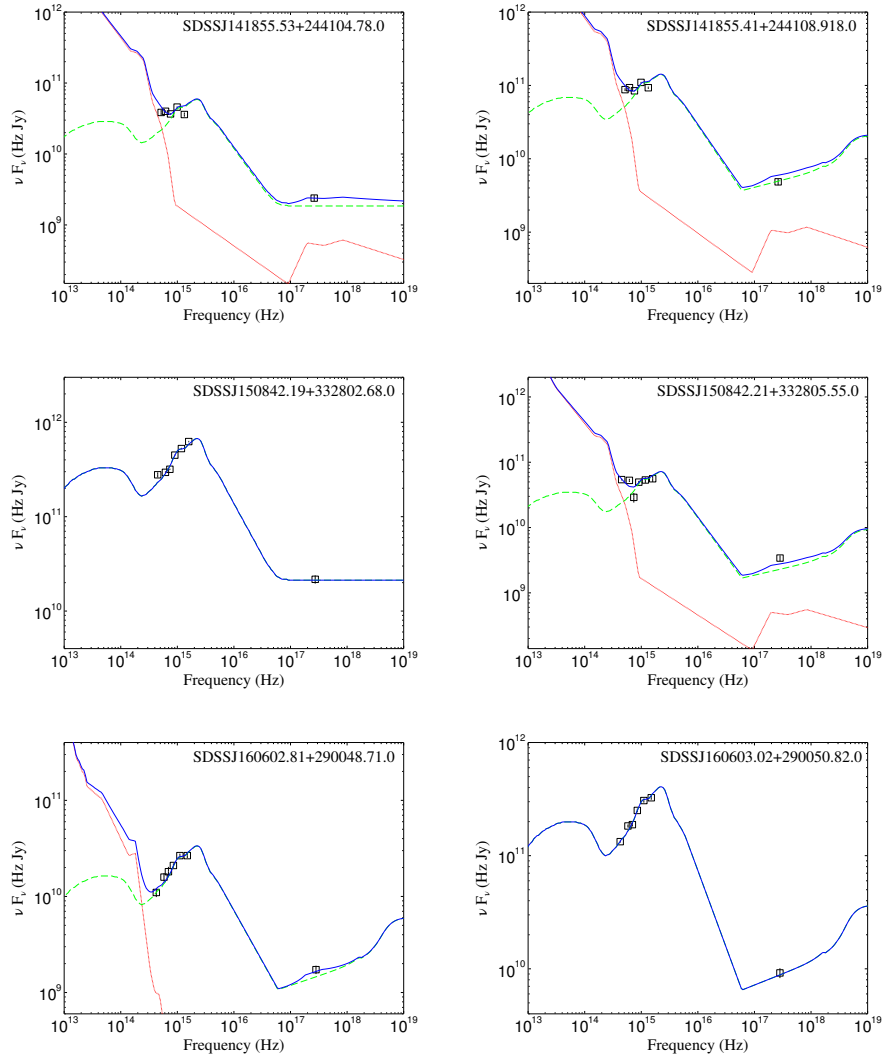


Fig. 5.— Near-infrared to X-ray SEDs (Ruiz et al. 2010) in  $\nu f_\nu$  for all our quasar pairs. Solid blue lines show the total predicted SED. Green and blue lines are the corresponding AGN and starburst templates used. Parameters for model fits are given in Table 4.

Table 2. Chandra Close Binary Quasar Sample

| SDSS NAME           | $r$ mag <sup>a</sup> | $z^b$      | Counts <sup>c</sup> | $\Gamma_{PL}^d$        | $\Gamma_{PLAbs}^d$     | $N_H^z$ <sup>e</sup> | $\log f_X^f$ | $\log l_X^g$ | $\alpha_{ox}^h$ |
|---------------------|----------------------|------------|---------------------|------------------------|------------------------|----------------------|--------------|--------------|-----------------|
| J074013.42+292645.7 | 19.47                | 0.978 H    | 82.4                | $1.85^{+0.20}_{-0.20}$ | $1.85^{+0.26}_{-0.20}$ | <27                  | -13.527      | 25.993       | 1.583           |
| J074013.44+292648.3 | 18.27                | 0.9803 S   | 288.5               | $2.24^{+0.11}_{-0.11}$ | $2.24^{+0.11}_{-0.11}$ | <9                   | -13.044      | 26.589       | 1.540           |
| J081312.63+541649.8 | 20.08                | 0.7814 M10 | 195.7               | $2.51^{+0.15}_{-0.14}$ | $2.51^{+0.15}_{-0.14}$ | <12                  | -13.414      | 26.006       | 1.426           |
| J081313.10+541646.9 | 17.18                | 0.7792 S   | 2336.8              | $1.90^{+0.06}_{-0.06}$ | $1.93^{+0.04}_{-0.04}$ | <1                   | -12.255      | 27.051       | 1.460           |
| J115822.77+123518.5 | 19.85                | 0.5996 M08 | 367.7               | $2.26^{+0.10}_{-0.10}$ | $2.51^{+0.19}_{-0.18}$ | $18^{+11}_{-11}$     | -13.098      | 26.017       | 1.335           |
| J115822.98+123520.3 | 20.12                | 0.5957 M08 | 413.6               | $2.16^{+0.09}_{-0.09}$ | $2.14^{+0.16}_{-0.14}$ | <9                   | -13.069      | 25.999       | 1.292           |
| J125454.86+084652.1 | 19.43                | 0.4401 G   | 349.5               | $2.11^{+0.10}_{-0.10}$ | $2.11^{+0.10}_{-0.10}$ | <2                   | -12.853      | 25.887       | 1.355           |
| J125455.09+084653.9 | 17.08                | 0.4392 G   | 1795.5              | $2.04^{+0.04}_{-0.04}$ | $2.04^{+0.04}_{-0.04}$ | <1                   | -12.129      | 26.597       | 1.431           |
| J141855.41+244108.9 | 19.21                | 0.5728 S   | 864.9               | $1.94^{+0.06}_{-0.06}$ | $1.99^{+0.11}_{-0.10}$ | <7                   | -12.692      | 26.305       | 1.282           |
| J141855.53+244104.7 | 20.13                | 0.5751 M08 | 33.0                | $0.72^{+0.28}_{-0.28}$ | $1.6^{+0.60}_{-0.54}$  | $158^{+113}_{-87}$   | -13.769      | 25.132       | 1.575           |
| J150842.19+332802.6 | 17.80                | 0.8773 S   | 1040.9              | $2.10^{+0.06}_{-0.06}$ | $2.10^{+0.06}_{-0.06}$ | <8                   | -12.670      | 26.807       | 1.514           |
| J150842.21+332805.5 | 20.19                | 0.878 H    | 111.1               | $2.37^{+0.45}_{-0.40}$ | $2.61^{+0.37}_{-0.20}$ | <27                  | -13.708      | 25.860       | 1.479           |
| J160602.81+290048.7 | 18.35                | 0.7701 S   | 6.1                 | $0.60^{+0.71}_{-0.73}$ | 1.8                    | <0.01                | -14.396      | 24.860       | 2.122           |
| J160603.02+290050.8 | 18.25                | 0.7692 M08 | 144.1               | $2.20^{+0.43}_{-0.42}$ | $2.44^{+0.17}_{-0.16}$ | <6                   | -13.171      | 26.222       | 1.611           |

<sup>a</sup>SDSS dereddened PSF magnitude.

<sup>b</sup>Redshift. M10 - Myers et al. (2010); M08 - Myers et al. (2008); H - Hennawi et al. (2006); G - Green et al. (2010); S - SDSS

<sup>c</sup>Net 0.5-8 keV counts.

<sup>d</sup>Best-fit X-ray power-law photon index. Uncertainties are the 68% confidence limits. If no uncertainties are shown, then the value is frozen to enable fitting of  $N_H^z$ .

<sup>e</sup>Best-fit intrinsic column for *PLAbs* model in units  $10^{20}$  cm<sup>-2</sup>. Upper limits are at 68% confidence.

<sup>f</sup>X-ray flux (0.5-8 keV) in erg cm<sup>-2</sup> s<sup>-1</sup> calculated using the *PLAbs* model.

<sup>g</sup>X-ray luminosity at 2 keV in erg s<sup>-1</sup> Hz<sup>-1</sup>.

<sup>h</sup> $\alpha_{\text{ox}}$ , the optical/UV to X-ray spectral index.

Table 3. Chandra Binary Quasar Sample Near-Infrared Properties

| SDSS Name           | Exposure <sup>a</sup> | $J_S$ <sup>b</sup> | err $J_S$ <sup>c</sup> | $J_U$ <sup>d</sup> | err $J_U$ <sup>e</sup> | Y <sup>f</sup> | errY <sup>g</sup> | H <sup>h</sup> | errH <sup>i</sup> | K <sup>j</sup> | errK <sup>k</sup> |
|---------------------|-----------------------|--------------------|------------------------|--------------------|------------------------|----------------|-------------------|----------------|-------------------|----------------|-------------------|
| J074013.42+292645.7 | ...                   | ...                | ...                    | ...                | ...                    | ...            | ...               | ...            | ...               | ...            | ...               |
| J074013.44+292648.3 | ...                   | ...                | ...                    | ...                | ...                    | ...            | ...               | ...            | ...               | ...            | ...               |
| J081312.63+541649.8 | 2610                  | 17.869             | 0.034                  | ...                | ...                    | ...            | ...               | ...            | ...               | ...            | ...               |
| J081313.10+541646.9 | 2610                  | 18.744             | 0.061                  | ...                | ...                    | ...            | ...               | ...            | ...               | ...            | ...               |
| J115822.77+123518.5 | 900                   | 17.174             | 0.013                  | ...                | ...                    | ...            | ...               | 17.085         | 0.050             | 16.239         | 0.036             |
| J115822.98+123520.3 | 900                   | 17.411             | 0.016                  | ...                | ...                    | ...            | ...               | 17.515         | 0.074             | 16.732         | 0.056             |
| J125454.86+084652.1 | 1260                  | 18.098             | 0.061                  | 17.925             | 0.045                  | 18.424         | 0.034             | 17.066         | 0.022             | 16.129         | 0.029             |
| J125455.09+084653.9 | 1260                  | 16.063             | 0.010                  | 16.079             | 0.009                  | 16.505         | 0.008             | 15.433         | 0.006             | 14.327         | 0.007             |
| J141855.41+244108.9 | ...                   | ...                | ...                    | ...                | ...                    | ...            | ...               | ...            | ...               | ...            | ...               |
| J141855.53+244104.7 | ...                   | ...                | ...                    | ...                | ...                    | ...            | ...               | ...            | ...               | ...            | ...               |
| J150842.19+332802.6 | 630                   | 16.551             | 0.058                  | 16.629             | 0.012                  | ...            | ...               | ...            | ...               | ...            | ...               |
| J150842.21+332805.5 | 630                   | 18.473             | 0.031                  | 18.463             | 0.063                  | ...            | ...               | ...            | ...               | ...            | ...               |
| J160602.81+290048.7 | ...                   | ...                | ...                    | 17.398             | 0.023                  | ...            | ...               | ...            | ...               | ...            | ...               |
| J160603.02+290050.8 | ...                   | ...                | ...                    | 17.369             | 0.022                  | ...            | ...               | ...            | ...               | ...            | ...               |

<sup>a</sup>total MMT-SWIRC exposure time in seconds

<sup>b</sup>SWIRC J-band magnitudes

<sup>c</sup>Error in SWIRC J-band magnitudes

<sup>d</sup>UKIDSS J-band magnitudes

<sup>e</sup>Error in UKIDSS J-band magnitudes

<sup>f</sup>UKIDSS Y-band magnitudes

<sup>g</sup>Error in UKIDSS Y-band magnitudes

<sup>h</sup>UKIDSS H-band magnitudes

<sup>i</sup>Error in UKIDSS H-band magnitudes

<sup>j</sup>UKIDSS K-band magnitudes

<sup>k</sup>Error in UKIDSS K-band magnitudes

Table 4: Quasar Spectral Energy Distribution Fit Results

| SDSS Name           | $\log L_{Bol}^a$ | $J_{AGN}^b$ | $J_{SB}^c$      | $P_{IRX}^d$ | $P_{Bol}^e$ |
|---------------------|------------------|-------------|-----------------|-------------|-------------|
| J074013.42+292645.7 | 46.362           | QSO         | ...             | 100/0       | 100/0       |
| J074013.44+292648.3 | 46.909           | QSO         | ...             | 100/0       | 100/0       |
| J081312.63+541649.8 | 48.159           | QSO         | M82             | 71/29       | <10/>90     |
| J081313.10+541646.9 | 47.087           | QSO         | NGC7714         | 79/21       | 79/21       |
| J115822.77+123518.5 | 47.185           | LDQSO       | IRAS 12112+0305 | 74/26       | <10/>90     |
| J115822.98+123520.3 | 45.770           | LDQSO       | NGC7714         | 58/42       | 58/42       |
| J125454.86+084652.1 | 45.787           | LDQSO       | ...             | 100/0       | 100/0       |
| J125455.09+084653.9 | 46.457           | QSO         | ...             | 100/0       | 100/0       |
| J141855.41+244108.9 | 48.009           | LDQSO       | IRAS 12112+0305 | 80/20       | <10/>90     |
| J141855.53+244104.7 | 47.713           | QSO         | IRAS 12112+0305 | 76/24       | <10/>90     |
| J150842.19+332802.6 | 47.013           | QSO         | ...             | 100/0       | 100/0       |
| J150842.21+332805.5 | 48.127           | LDQSO       | IRAS 12112+0305 | 77/23       | <10/>90     |
| J160602.81+290048.7 | 48.225           | LDQSO       | M82             | 68/32       | <10/>90     |
| J160603.02+290050.8 | 46.641           | LDQSO       | ...             | 100/0       | 100/0       |

<sup>a</sup>log of the luminosity from  $10^9$  -  $10^{19}$  Hz in units of  $\text{erg s}^{-1}$  from template fit

<sup>b</sup>AGN template used in the best fit solution: QSO (radio quiet QSO), LDQSO (luminosity-dependent

<sup>c</sup>Starburst template used in the best fit

<sup>d</sup>Percent QSO/starburst contribution in the range  $10^{14}$  -  $10^{18}$  Hz

<sup>e</sup>Percent QSO/starburst contribution in the range  $10^9$  -  $10^{19}$  Hz